Fast Surface-Plasmon-Mediated Electro-Optics of a Liquid Crystal on a Metal Grating

M. V. Gorkunov,[1,2] I. V. Kasyanova,[1] V. V. Artemov,[1] M. I. Barnik,[1] A. R. Geivandov,[1] and S. P. Palto[1]

[1]*Shubnikov Institute of Crystallography, Federal Scientific Research Centre "Crystallography and Photonics," Russian Academy of Sciences, 119333 Moscow, Russia*

[2]*National Research Nuclear University MEPhI (Moscow Engineering Physics Institute), 115409 Moscow, Russia*

(Received 12 January 2017; revised manuscript received 20 June 2017; published 30 November 2017)

Combined with liquid crystals, plasmonic nanostructures acquire voltage-driven optical tunability. We report that light-transmitting interdigitated aluminum grating covered with a nematic liquid crystal exhibits fast electro-optical switching: for the visible light wavelengths above the surface-plasmon resonance, its switching is thresholdless and, being driven by a voltage of a few volts, occurs on a time scale of tens of microseconds. We relate these features to the fast liquid crystal realignment within a thin surface layer that controls the plasmon excitation and light transmission.

DOI: 10.1103/PhysRevApplied.8.054051

I. INTRODUCTION

The emergence of advanced nanofabrication techniques has facilitated the development of metallic optical materials that are finely structured on the scale below the visible-light wavelengths. Such materials host an impressive range of electromagnetic phenomena which are prospective for numerous photonic applications: plasmon resonances that concentrate the light energy at metal tips and edges and strongly enhance the Raman scattering [1] and other nonlinear processes [2]; extraordinary light transmission through holes [3] and slits [4] utilized for light polarizing and color filtering [5,6]; and strong [7] and extremely strong [8] optical chirality, which, in combination with the sensitivity to the nanoscale environment, enables the chirality sensing [9] and biosensing [10], to name a few.

From similar constituent materials, one can obtain metallic nanostructures with very different optical properties by choosing the appropriate shape and size for the metal parts. Upon production, however, the rigid structures can hardly be modified by reasonable physical factors. Since reconfigurability and dynamical control of the optical response are desirable for most optical applications, much effort has been put into the development of tunable hybrid metamaterials [11]. The advantages of tunability acquired by metal-dielectric structures from a flexible liquid crystal (LC) environment, in particular, have been repeatedly demonstrated [12–20].

For many decades, it has been clear that realigning anisotropic LCs in the vicinity of a plain metal surface substantially affects plasmons traveling along it [21,22], and related devices such as a LC-based plasmonic spatial light modulator [23] have been proposed. Early experiments with subwavelength metallic structures on the substrates of nematic LC cells already showed that the voltage-driven switching of the LC environment could also noticeably affect the extraordinary light transmission [12] and could shift the localized plasmon resonances [13]. Infiltrating more sophisticated multilayer metamaterials with LCs also enabled the tuning by temperature [14] and laser radiation [15]. While metal conductivity facilitates the use of the nanostructures as electrodes, nanostructures have other valuable features and can also act as polarizers [16,17] and efficient LC alignment layers [16,18].

In a majority of cases, LCs are employed in the geometry of a standard twisted-nematic LC cell (see, e.g., Refs. [16,17]), when the voltage drop between the metal structure and the opposite substrate creates an electric field that drives the LC bulk from the twisted to the homeotropic state [24,25]. Recently, a notable extension of the optical reflection geometry was also reported [20]. In very recent works [18,19], a more advanced in-plane–switching (IPS) LC cell design was used in which the switching voltage was applied to the interdigitated metal electrodes on the same substrate and an analog of the in-plane–switching transition [26] was observed.

Although using the established cell designs ensures reliable LC behavior, the electro-optics of such LC-metamaterial hybrids remains very similar to conventional LC-display cells. From a practical viewpoint, the sophisticated nanostructures effectively replace common polarizing and spectral filtering elements, which substantially increases the technological complexity but hardly provides alternative performance features or improves the operating characteristics.

Generally, immersing optical metallic nanostructures in LCs can result in very different nonstandard switching geometries. Thus, it has been pointed out that applying voltage across a subwavelength array of parallel metal wires—a wire-grid metamaterial—surrounded by a nematic LC creates rather specific LC director patterns and enables low-voltage tunability of the effective metamaterial permittivity [27].

In this paper, we report on the experimental realization of a two-dimensional hybrid metamaterial composed of a planar interdigitated aluminum nanograting covered with a nematic LC. Our recent experiments have indicated that its visible transmission is tunable by voltage [28]. Here, we demonstrate that, by using such hybrid systems beyond standard LC cell geometry, one can substantially enhance the electro-optical performance: the speed exceeds that typical of the cells of the same thickness and LC material by several orders of magnitude, while the switching is thresholdless and requires voltages of a few volts. Based on the polarized grating transmission spectra, we determine the peculiar alignment patterns of the LC adjacent to the grating, while the analysis of the precisely resolved switching dynamics unveils the details of the switching scenario. Comparing the experimental data to the numerical simulation results, we are able to identify that the switching is mediated by the surface plasmons: being sensitive to subtle variations of the LC alignment in the nanoscale vicinity of the metal surface, they determine the visible grating transmission.

II. HYBRID LIQUID CRYSTAL CELL

A schematic design of the hybrid LC cell is given in Fig. 1. The top substrate is standard optical display-grade glass covered with a thin rubbed polyimide layer providing planar LC surface alignment. The bottom substrate is a fused silica plate with a 70-nm thin aluminum layer deposited by thermal vacuum sputtering.

The interdigitated grating is patterned in aluminum by means of the focused ion beam (FIB) milling using an FEI Scios dual-beam electron microscope. To facilitate the milling, a relatively large current of 0.3 nA of gallium ions of an energy of 30 keV is used. The milling procedure is controlled by digital templates, which allow us to produce (40×40)-μm^2 large interdigitated grating samples with a period of $\Lambda = 400$ nm and a slit width $w \approx 100$ nm, as illustrated in Fig. 2(a). Note that the total slit length exceeds 4 mm, and not a single electric contact is detected across it. Electrical insulation of the interdigitated electrodes is achieved by extending the meander slit from both sides of the grating by FIB-milled line cuts, which are further extended by wider laser-made cuts far enough from the grating. Separately, a square window of the same size is milled in the aluminum for optical reference purposes.

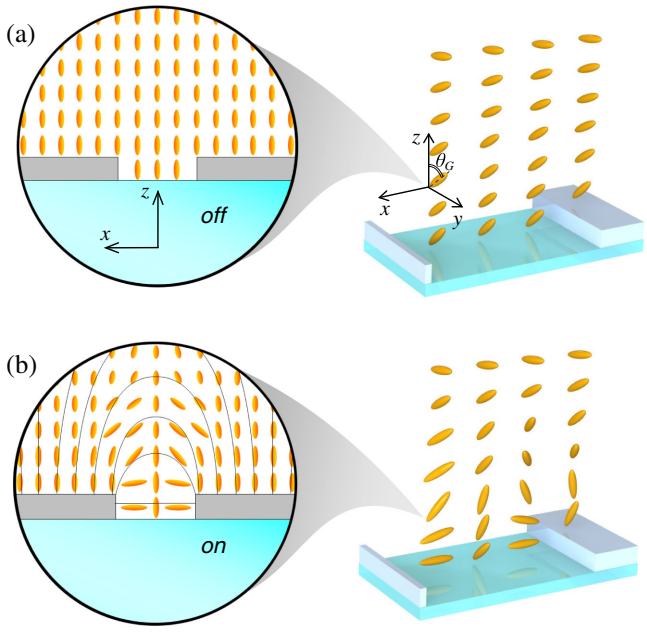

FIG. 1. Hybrid LC cell with an interdigitated plasmonic grating. The LC alignment is shown in the (a) *off* and (b) *on* states with the enlarged views of the LC layers adjacent to the grating. The electric-field lines are schematically depicted by thin black lines in (b). Note that the relative sizes of the LC molecules, the grating dimensions, and the LC cell thickness are out of proportion.

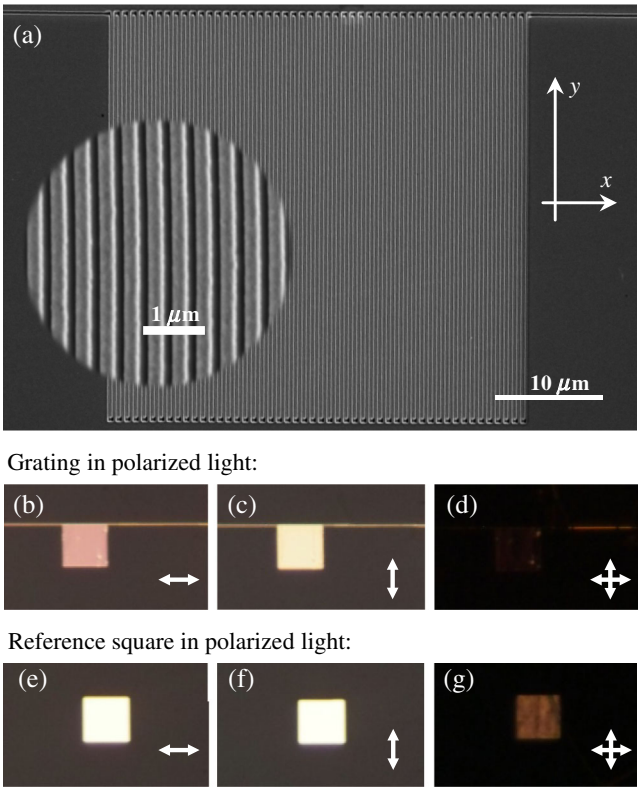

FIG. 2. Interdigitated plasmonic grating milled by a focused ion beam in a 70-nm thin aluminum film on a fused silica substrate. (a) A SEM image of the whole grating and an enlarged view of part of it. Optical images of the grating (b) inside a LC cell illuminated by the light polarized across the grating strips (TM polarization), and (c) along the strips (TE polarization). (d) The grating as viewed between the orthogonal polarizers (TM polarizer and TE analyzer). (e)–(g) The polarized optical images of the reference square are shown below the corresponding grating images. All of the optical images are obtained under the same input illumination and camera exposure settings.

The LC cell is assembled with a 3-μm gap between the substrates ensured by Teflon film spacers. The gap is infiltrated with a commercial Merc E7 LC mixture that exhibits a stable nematic phase at room temperature. Monitoring of the LC cell in polarized light is used to assess the quality of the LC alignment. Taking the rubbing direction of polyimide on the top substrate along the strips of the grating on the bottom substrate allow us to stabilize the whole LC layer over the grating area, as seen in the optical images in Figs. 2(b) and 2(c). The grating role is significant, as it provides a much better LC alignment than that formed above the square reference window [compare Figs. 2(d) and 2(g)].

To extract more quantitative information on the LC alignment, polarized optical transmission measurements are performed using a setup with Olympus CX31PF-5 (U-CTR 30-2) trinocular polarized-light microscope and a Moxtek UBB01A ultrabroadband wire-grid polarizer. The microscope halogen lamp is used as a light source in a wide range (350–1000 nm), and the spectral composition of the transmitted light is resolved using fiber-optic Avantes AvaSpec-2048-USB2-UA spectrometer attached to the microscope.

The obtained TM-polarized (that is, the light magnetic field is in the y direction along the slits) normal-incidence transmittance spectra exhibit pronounced dips (see Fig. 3), which are very typical for metal slit gratings. The transmittance of the bare grating on a fused silica substrate has minima at wavelengths of 418 and 615 nm. For the grating inside the LC cell, the short-wavelength minimum is absent while the long-wavelength one remains and, being masked by the oscillating interference pattern of the Fabry-Perot effect within the LC cell, appears to be split into a pair of minima at 575 and 625 nm.

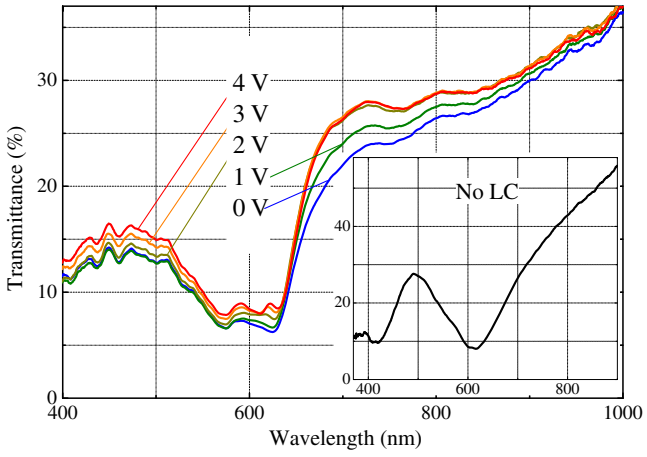

FIG. 3. Spectra of the TM-polarized light transmission of the aluminum grating inside a LC cell upon different voltages (from 0 to 4 V, as indicated) applied to the interdigitated grating electrodes. (Inset) The transmission of the bare grating on a fused silica substrate. All spectra are normalized by the transmission of an empty square aperture of the same dimensions.

Such TM-polarized transmission dips are known to be related to the surface plasmons on the grating [29,30]. Specifically, the transmission drastically drops down and the reflection reaches high values typical for flat metal mirrors when the wavelength of light incident normally on the grating approaches

$$\lambda_j^{(i)} = \frac{\Lambda}{j}\mathrm{Re}\left[\sqrt{\frac{\varepsilon_m\varepsilon_i}{\varepsilon_m+\varepsilon_i}}\right], \tag{1}$$

where j is a nonzero integer, Λ is the grating period, and ε_m and ε_i are the permittivities (generally complex) of the grating metal and its ith substrate, respectively [29].

The transmission spectrum of the grating on the fused silica substrate shown as an inset in Fig. 3 perfectly exemplifies this general rule. The minimum observed at the 418-nm wavelength is close to $\lambda_1^{(\mathrm{air})} \approx 411$ nm, as evaluated for $j = 1$, $\Lambda = 400$ nm, $\varepsilon_{\mathrm{air}} = 1$, and the complex aluminum permittivity around this wavelength, $\varepsilon_{\mathrm{Al}} = -18.7 + 3.44i$, in accordance with the experimental data [31]. The position of the other minimum at 615 nm is also close to $\lambda_1^{(\mathrm{fs})} \approx 598$ nm evaluated for the permittivities $\varepsilon_{\mathrm{fs}} = 2.13$ of fused silica [32] and $\varepsilon_{\mathrm{Al}} = -39.6 + 12.6i$ of aluminum [31] in this range. We attribute weak deviations of the minimum positions to the uncertainties of the grating period Λ (the spatial precision of FIB fabrication is at the 5% level) and of the aluminum permittivity values, which are known to alter substantially from sample to sample due to, e.g., partial aluminum oxidation [31,33]. Note also that, in theory, the transmission drops to very low values below the 1% level. We relate the observed 7% minimum levels to the transmission of light depolarized by the roughness of the aluminum grating strips and to the light tunneling through the top and bottom meander and side cuts of the grating.

As seen in Fig. 3, in agreement with Eq. (1), the short-wavelength minimum disappears when the grating is inserted into the LC cell and the air-grating interface is replaced by the LC-grating one. The high-wavelength minimum is split, as the LC and silica permittivities have relatively close values, which provides a convenient way of estimating their difference. Indeed, in the first approximation, a small relative variation of the substrate permittivity gives rise to a proportionate relative shift of the wavelength (1): $\delta\lambda^{(i)}/\lambda^{(i)} = \delta\varepsilon_i/2\varepsilon_i$. Accordingly, a 50-nm split of the plasmon wavelengths corresponds to a relative difference of about $1/6$ between the LC and silica permittivities. From the tabulated silica data [32], $n_{\mathrm{fs}} = 1.458$ and $\varepsilon_{\mathrm{fs}} = 2.13$, we obtain the effective value of the LC permittivity as $\varepsilon_{\mathrm{LC}}^{\mathrm{eff}} \approx 2.48$. As it equals neither of the main values of the permittivity tensor of the chosen E7 LC compound ($n_o = 1.52$, $\varepsilon_o = 2.31$ and $n_e = 1.74$, $\varepsilon_e = 3.03$ [34]), this result provides strong evidence for a tilted LC orientation at the grating.

Note that, in the majority of works on LC-covered metamaterials (see, e.g., Refs. [16–20,27,28]), the planar LC alignment on metal nanostructures is assumed *a priori*. For independent verification of the pretilted LC orientation, we analyze the TE-polarized transmission spectrum, which is far less peculiar and stays at the 40% level in the visible range, with a pronounced periodic modulation due to the Fabry-Perot interference within a few-micron-thick LC layer (seen also in the short- and long-wavelength tails of the TM-polarized transmission in Fig. 3). A Fourier transform of the spectra allows us to obtain the optical thickness of the LC layer for the TE-polarized light as $L_{\mathrm{TE}} = 4.24\ \mu$m.

Next, measuring the optical retardation at a 546-nm wavelength using the Berek compensator within the same microscope setup allows us to determine the difference between the optical paths of the TE- and TM-polarized light as $R = L_{\mathrm{TE}} - L_{\mathrm{TM}} = 0.36\ \mu$m. Since the path of the TM-polarized light is determined by $n_{\mathrm{LC}}^{\mathrm{TM}} = n_o$, we conclude that the actual LC cell thickness is $d = 2.55\ \mu$m, and the average refractive index of the LC layer for the TE-polarized light is $n_{\mathrm{LC}}^{\mathrm{TE}} = 1.66$.

Rubbed polyimide on the top substrate is a standard coating that provides an almost planar alignment of the adjacent LC. In the cell bulk, the LC elastic deformation energy is minimized when the director tilt angle varies smoothly with the coordinate z, as shown in Fig. 1(a). By solving numerically the one-dimensional problems for the director distribution and light propagation, we learn that the obtained average value of $n_{\mathrm{LC}}^{\mathrm{TE}}$ corresponds to the alignment depicted in Fig. 1(a) with $\theta_G \approx 30°$, which provides independent proof that the LC alignment at the grating is indeed very far from planar.

III. ELECTRO-OPTIC EFFECT

Next, different voltages are applied to the interdigitated grating, and the transmitted light spectra are recorded in the trigger mode at an interval of 10 ms after the leading front of the trigger pulse. Electric voltage pulses with a duration of 10 ms and a repetition frequency of 20 Hz are applied synchronously with the trigger pulses to the interdigitated electrodes of the subwavelength aluminum grating.

As seen in Fig. 3, applying the voltage noticeably alters the transmittance. The electro-optic effect differs qualitatively in various parts of the visible-light spectrum. At shorter wavelengths, low voltages produce a very subtle effect on the transmission, as it is affected only when the voltage U exceeds 2 V. At longer wavelengths, the opposite is true: the transmission undergoes distinct variation at $U \leq 2$ V and remains unaffected by further increase of the voltage. This peculiar behavior allows us to extract key qualitative information on the LC switching.

As discussed above, the optical transmission data indicate that, until the voltage is applied, the LC director is aligned in the z-y plane rotating from the planar orientation at the top substrate to that tilted by a substantial angle θ_G at the grating [see Fig. 1(a)]. When the voltage is applied across the grating slits, it produces an inhomogeneous electric field which is neither parallel nor perpendicular to the local initial LC director orientation [see the field lines in Fig. 1(b)] and exerts torque on the LC molecules. In contrast to conventional IPS, this torque does not occur in the whole LC volume but instead is localized close to the slits, and it vanishes at distances of a few hundred nanometers from the grating. Accordingly, by increasing the voltage, one directly affects the LC orientation only within this thin layer. The LC bulk is then perturbed indirectly by propagating elastic deformation. This perturbation of the LC bulk by higher voltages manifests itself in Fig. 3 through the transmission changes at shorter wavelengths, when the normally incident light undergoes diffraction on the grating and propagates through the LC layer as a combination of several plane waves (zeroth-order transmission and two diffracted waves). The orientation of LC in the bulk determines their relative retardation and interference and alters the observable transmission accordingly.

At larger wavelengths, in the absence of light diffraction, the hybrid LC cell operates in the so-called subwavelength grating regime, and the retardation of a single wave propagating through the LC cell does not directly affect the transmission. Here, the electro-optics is in fact very unusual: the transmittance is very sensitive to small voltages, as its modulation reaches 2.3% for the voltage $U = 1$ V and then remains close to 5% for $U = 2$ V and higher. One can explain this peculiar behavior by suggesting that the transmission is weakly sensitive to the LC bulk being mainly determined by the alignment of the LC layers adjacent to the grating. Precisely those LC layers control the properties of surface plasmons on the grating-LC interface, which indicates that the observed electro-optics in the subwavelength regime is likely to be plasmon mediated. As is discussed in Sec. V, the particular mechanism is not so trivial, however. In the absence of direct methods that could resolve LC alignment on such scales, one can draw an analogy with conventional IPS and suggest the LC pattern shown in Fig. 1(b). As is typical for the IPS geometry [35,36], the LC molecules tend to orient parallel to the electric-field lines, away from those that are directly above the slit middle. Numerical modeling of the LC alignment discussed in Sec. V indeed confirms that the LC molecules there remain orthogonal to the electric field.

IV. SWITCHING DYNAMICS

The precise dynamics of the electro-optical switching is resolved using a Si 650-nm lasing photodiode mounted to the port of the Olympus microscope instead of the optical fiber of the Avantes spectrometer. The custom-designed electrical circuit of the photodiode allows for both high sensitivity (approximately 10^{-10} W in a frequency band of 1 MHz) and a submicrosecond response time. The signal

from this detector is registered with the help of the virtual digital oscilloscope of PHYSLAB software (custom design) using a 16-bit analog-to-digital converter with a 2-μs time resolution. The PHYSLAB digital oscilloscope is used in accumulation mode, so the electro-optical response is averaged synchronously with the voltage pulses generated by a PHYSLAB arbitrary waveform generator. The voltage waveform from the 14-bit digital-to-analog converter of the generator is amplified by a wideband frequency amplifier and applied to the grating electrodes. The synchronous averaging allows for an extremely wide dynamic range (more than 5 orders in magnitude) with low noise levels. The latter is extremely important when a narrow diaphragm (approximately 0.5 mm in diameter) is placed in front of the photodiode in order to restrict the photodiode field of view by a size of about 50 μm that is comparable to the size of the studied gratings (40 μm).

The summary of the obtained electro-optical switching dynamics is given in Fig. 4. For clarity, all of the curves are normalized to the same transmission level when the voltage-driven effects are stabilized. The absolute modulation depth of the transmittance is indicated for several cases in Fig. 4(b). Although the wavelength of 650 nm does not correspond to the strongest electro-optical effect (see Fig. 3), the modulation depth here follows the general trend: being sensitive to the voltages below 2 V, it remains much less affected by higher voltages. The transmission switching fronts can be well approximated with single-exponential fits typical for LC electro-optics in various geometries [24,25]:

$$\Delta T_{\mathrm{on}}(t) \propto \exp\left(-\frac{t-t_{\mathrm{on}}}{\tau_{\mathrm{on}}}\right) \tag{2}$$

for the switching on, and

$$\Delta T_{\mathrm{off}}(t) \propto -\exp\left(-\frac{t-t_{\mathrm{off}}}{\tau_{\mathrm{off}}}\right) \tag{3}$$

for the switching off, where t_{on} and t_{off} are the moments when the voltage is applied and removed, respectively, and τ_{on} and τ_{off} are the corresponding switching times.

As seen in Fig. 4, for the voltages up to 2 V, the dynamics precisely follows the simple dependences (2) and (3). At higher voltages, substantial deviations occur: the switched-on transmission relaxes to lower values after the initial fast growth, and the switching-off front becomes distinctively nonexponential.

The switching times resolved by the fitting are summarized in Fig. 5(a). One can see that the switching-off time stays at a level of 120-140 μs almost independently of the driving voltage. The switching-on time remains of the same value for the voltages of 2 V and below. For the higher voltage, it rapidly drops down and eventually goes below the 20-μs level.

Such dependences of the switching times on driving voltage are typical for various LC systems, and simple models describing one-dimensional LC deformations yield the switching-off (relaxation) time as the ratio of the LC viscosity coefficient γ to the characteristic density of the LC elastic deformation energy [25,26]:

$$\tau_{\mathrm{off}} = \frac{\gamma}{Kq^2}, \tag{4}$$

where K is the elastic constant of the relevant LC deformation, and q is the deformation wave number. For the Merck E7 LC mixture used in our experiments,

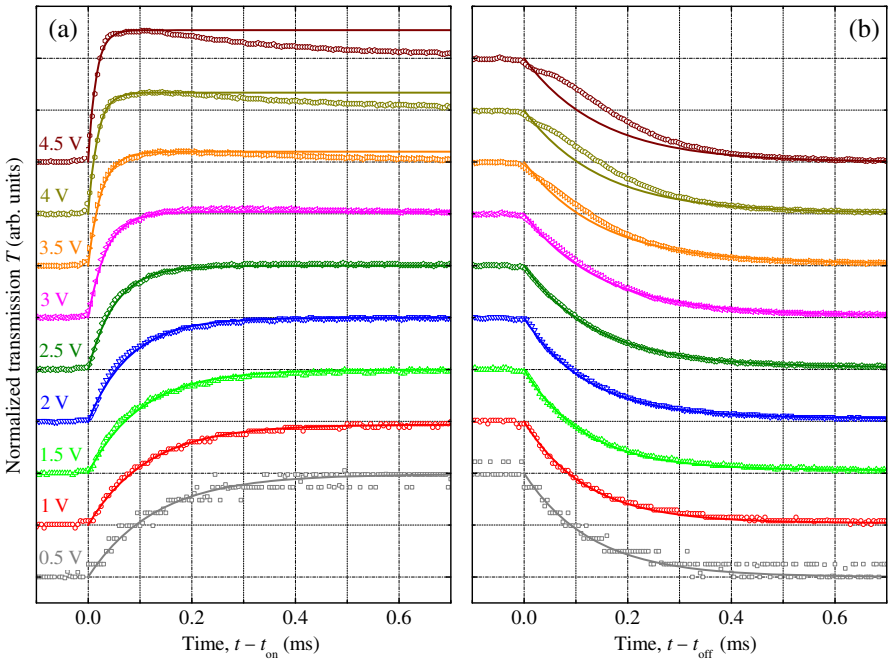

FIG. 4. Dynamics of the electro-optical (a) switching on and (b) switching off of the hybrid LC cell transmission at a wavelength of 650 nm for a driving voltage varying from 0.5 to 4.5 V (as indicated). All transmission profiles are normalized to the values stabilized in the *on* state. Absolute transmission variation at the 650-nm wavelength according to the data shown in Fig. 3 is indicated in (b). Solid lines correspond to the best fits with the single-exponential equations (2) and (3).

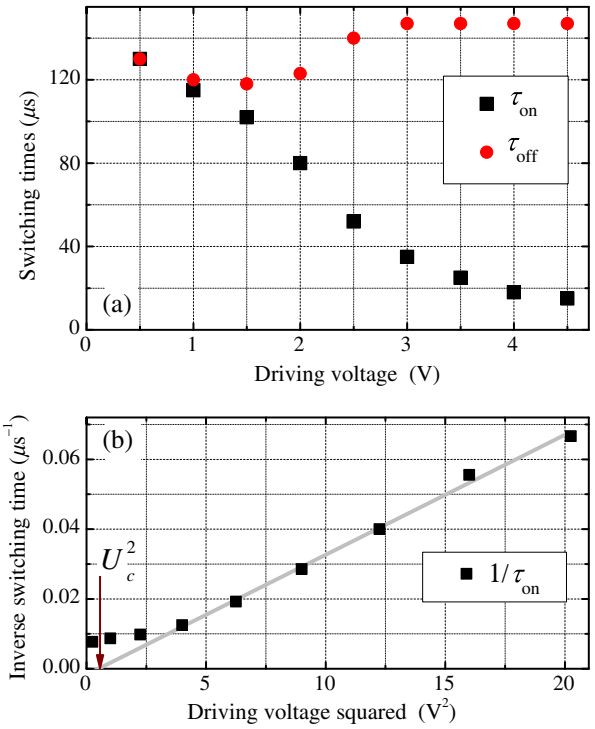

FIG. 5. (a) Electro-optical switching times resolved by single-exponential fitting of the switching dynamics as shown in Fig. 4. (b) Dependence of the inverse switching-on time on the squared voltage, and its best linear fit (the solid line) at higher voltage.

$\gamma \approx 0.19$ Pa s, and the elastic constants $K_{1,2,3}$ of the splay, twist, and bend deformations are 11, 9, and 17 pN, respectively [37]. The LC alignment in Fig. 1(b) includes all three deformation types. As those with higher elastic constants relax faster, the observed switching-off time in such a case is mainly determined by the relaxation of the softest slowly relaxing deformation mode, i.e., by the twist deformation. Accordingly, we set $K = 9$ pN in Eq. (4) and conclude that the observed relaxation time of about 120 μs corresponds to the characteristic deformation scale $L = 2\pi/q \sim 470$ nm. Being very approximate, this estimate is reasonably close to the grating period $\Lambda = 400$ nm, which determines the spatial scale of the deformation pattern depicted in Fig. 1(b).

In the frame of the classical field-induced LC switching transition, one can also express the switching-on time as the ratio of the LC viscosity to the benefit of the LC energy density [25,26]:

$$\tau_{\mathrm{on}} = \frac{\gamma}{\varepsilon_0 |\chi_a| \nu E^2 - K q^2}, \tag{5}$$

where ε_0 is the electric constant and χ_a is the low-frequency LC dielectric anisotropy. While, in the classical case, the switching field acts homogeneously on the whole LC layer, in our case, the driving electric field E more strongly affects the LC adjacent to the grating slits. Accordingly, we introduce in Eq. (5) the dimensionless parameter ν indicating the relative part of the LC-layer area affected by the electric field. Since the latter is proportional to the voltage applied across the slits $E \approx U/w$, Eq. (5) determines the voltage-dependent switching-on time as

$$\tau_{\mathrm{on}} = \frac{\gamma w^2}{\varepsilon_0 |\chi_a| \nu (U^2 - U_c^2)}, \tag{6}$$

with the critical voltage $U_c = qw\sqrt{K/|\chi_a|\nu\varepsilon_0}$.

In order to understand the applicability of Eq. (6), we plot in Fig. 5(b) the experimental values of the inverse switching-on time versus the squared voltage. Apparently, at voltages higher than 2 V, the dependence is perfectly linear, as implied by Eq. (6). The linear fit reveals an effective critical voltage of $U_c = 0.71$ V and, taking the known value of the E7 LC dielectric anisotropy $\chi_a = 13.8$ [37] and other parameters as mentioned above, we obtain the parameter $\nu \approx 0.36$. Thus, effectively about one third of the LC area above the grating is exposed to the driving electric field. This is what one expects, as the field indeed is much stronger inside and above the slits, i.e., within a third of the whole grating area.

For the driving voltages below 2 V, the observed switching times strongly deviate from the predictions of Eq. (6). Instead of critical slowing down as U approaches U_c, the system switches in both directions with almost the same speed. No switching threshold is seen and, in fact, a substantial part of the transmission variation is achieved at $U \leq U_c$ (see Fig. 3). It is quite consistent with the fact that the Frederiks transition threshold arises due to the orthogonality of the initial director orientation and the driving electric field and the ambiguity between the two possible LC deformations that determines a bifurcation accompanied by a critical switching regime. In our case, the initial LC director and the electric field form rather complex patterns above the grating, and their strict orthogonality occurs only eventually at some points. Accordingly, the absence of deformation ambiguity determines the continuous character of the switching transition.

V. NUMERICAL SIMULATIONS

To reveal the mechanism of fast electro-optic switching and to understand its potential for light modulator applications, we perform numerical simulations of the hybrid LC-plasmonic system, which includes modeling of the LC alignment above the metal grating, evaluating the TM-polarized transmittance spectra, and calculating the LC dynamic realignment upon applying voltage pulses across the grating slits.

Simulations of the LC alignment are performed using the LCDTDK software package developed by one of the authors (S. P. P.), which is capable of obtaining spatial distributions of the LC director $\mathbf{n}(\mathbf{r})$ in complex environments and under

the action of electric fields. It is based on solving dynamic 3D equations of the continuum LC mechanics and provides reliable results (see, e.g., Refs. [18,38]).

Generally, such continuous-medium simulations strongly rely on the boundary conditions imposed on LC material at the interfaces. Mathematically, such conditions can be conveniently described within appropriate models of the surface anchoring of the LC director [25]. It is established that the aligning action of rubbed polyimide is adequately described by infinitely strong anchoring that tends to orient the adjacent LC molecules almost in parallel to the substrate along the rubbing direction. On the other substrate of the hybrid system, the surface LC molecules are likely to experience uneven local conditions that are substantially different on the metal grating bars and upon the grating slits. As it is not feasible to extract the relevant microscopic parameters directly, we introduce effective boundary conditions while assuming infinitely strong anchoring that tends to align the surface layer of the LC molecules homogeneously tilted by an angle θ_G with respect to the surface normal. As described in Sec. II, one can adequately interpret the polarized optical transmission measurements within this model by assuming considerably large values of the tilt angle, $\theta_G \simeq 30°$.

For the simulations, we take the material parameters of the E7 nematic LC mixture mentioned in Sec. IV. The calculated smooth LC director distribution formed under the competing actions of the planar and tilted anchoring on the opposite substrates (the field *off* state) is shown in the left panel of Fig. 6. The director here is aligned in the y-z plane with $n_x = 0$. When the voltage is applied to the grating, strong orientational deformations occur inside and above the slits, where the induced electric field is maximal. The corresponding director distribution is shown in the right panel of Fig. 6 (the field *on* state). One can see distinct vertical walls exactly in the middle of the slits, where the initial director orientation is preserved. Emergence of such walls is typical for the IPS geometry [35,36], and their stability becomes apparent as one notes that, to the different sides of each wall, the director rotates away from the y-z plane in the opposite directions producing elastic torques that tend to rotate the LC molecules in the middle about the z axis in the opposite directions and, thus, cancel each other out. The electric field acting on the molecules here is exactly orthogonal to the LC director and also exerts no torque.

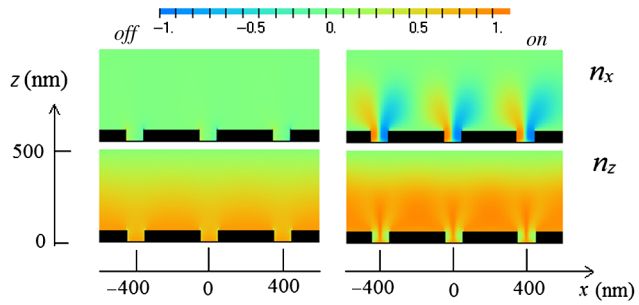

FIG. 6. Calculated LC director distributions (the n_x and n_z components shown as color maps) in the electric field *off* and *on* states. The electric field *on* state corresponds to the time moment 100 μs after the voltage pulse ($U = 3$ V) is applied. The calculations are done for a LC layer with a thickness of 0.5 μm with the planar alignment at the top surface and are tilted by $\theta = 30°$ in the y-z plane at the grating.

Next, the calculated LC director distributions are used to simulate the light transmission properties using the OPTIFDTD solver by Optiwave [39], which utilizes the finite-difference-time-domain method to solve the Maxwell equations. A built-in data set of aluminum properties includes the Lorentz-Drude dispersive model based on five resonances reproducing the tabulated frequency dispersion [33], which is generally in line with a more-recent characterization of high-quality aluminum films [31]. As in the optical experiments, the simulated grating has a period of $\Lambda = 400$ nm, and a slit width of $w = 100$ nm. We perform the 2D calculations in an x-z domain with a size of 10×20 μm. The light is normally incident from the fused silica substrate (with a refractive index $n = 1.46$) and the virtual sensor is located at a distance of 17 μm from a 10-μm-wide grating, which excludes the contribution from diffracted waves at shorter wavelengths.

Figure 7 shows the TM-polarized light-transmittance spectra calculated for the LC director distributions under different boundary conditions on the grating-LC interface. The Fig. 7 inset demonstrates the transmittance spectrum of the bare grating on a fused silica substrate with two

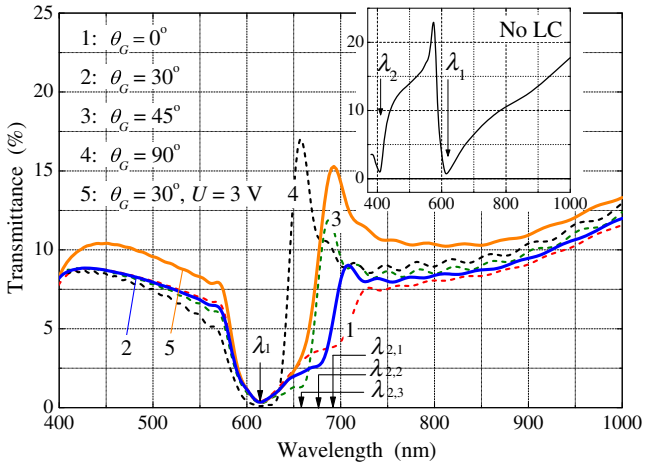

FIG. 7. Simulated transmittance spectra. Curves 1–4 correspond to different tilt angles θ_G of the LC director at the grating surface in the y-z plane, as indicated in the legend. Curve 5 illustrates the transmittance when the electric field ($U = 3$ V) is applied to the grating with the initial LC tilt of $\theta_G = 30°$. (Inset) The calculated transmittance of a bare grating on a fused silica substrate.

characteristic dips, at $\lambda_1 = 612$ nm and $\lambda_2 = 407$ nm, which are also observed experimentally and, as discussed in Sec. II, are related to the excitation of surface plasmons on the aluminum-substrate and aluminum-air interfaces, respectively.

As one can see in Fig. 7, the transmittance spectra substantially depend on the angle of the LC director tilt at the grating (curves 1–4). Specifically, while immersion into LC does not affect the position of the transmittance dip at $\lambda_1 = 612$ nm, the second dip is determined by the plasmonic properties of the grating-LC interface, and it occurs at $\lambda_{2,1} = 692$ nm, $\lambda_{2,2} = 676$ nm, and $\lambda_{2,3} = 658$ nm for $\theta_G = 0°$, 30°, and 45°, respectively. Since, in the surface plasmon excited in this geometry, the z component of the electric field is dominant, one can approximately identify the permittivity ε_i in Eq. (1) with the zz component of the permittivity tensor of the nematic LC tilted by θ_G: $\varepsilon_{\mathrm{LC}}^{\mathrm{eff}} \approx \varepsilon_o + (\varepsilon_e - \varepsilon_o)\cos^2\theta_G$. With the tabulated aluminum [33] and E7 [34] permittivities and the grating period of $\Lambda = 400$ nm, Eq. (1) yields, for the above set of tilt angles, the set of the surface-plasmon wavelengths of 710, 688, and 665 nm, which is in good agreement with the above numerically obtained $\lambda_{2,1-3}$.

Taking for the sake of clarity the initial LC state with $\theta_G = 30°$, we simulate the optical transmittance for the LC configuration under the competing actions of the surface forces and electric field (curve 5 in Fig. 7). One can see that the most vivid field-induced transmittance variation occurs within the range 650–700 nm. Qualitatively, the effect of the electric field there appears to be similar to an increase in θ_G (compare curves 5 and 3). We conclude that despite very complicated LC director patterns, one can interpret the transition from the field *off* to the field *on* spectra in terms of field-induced effective tilting of the LC director. The corresponding shift of the transmittance dips can be understood as a consequence of the surface-plasmon wavelength shift, and one can treat this electro-optical effect as "plasmon mediated."

Using the LCDTDK package, we also simulate the dynamics of the LC transitions between the field *off* and *on* states upon applying square-shaped voltage pulses across the grating slits. Evaluated switching of the LC director components at different distances above the fused silica substrate peculiarly shows an independence of the characteristic switching times of the position: the characteristic relaxation (switching-off transition from the field *on* to the field *off* state) time stays close to 100 μs until the distance becomes larger that 200 nm and the relaxation of the director z component slows down. Such a low dispersion of the relaxation times is determined by the existence of the domain walls in the middle of each slit. Our simulations in other geometries, where the walls do not appear, show a significant dispersion of the director relaxation times along the z direction just above the electrodes. Therefore, the domain walls effectively establish the grating period as the characteristic scale L of the LC deformations up to the distances of a few hundred nanometers above the grating. As the observable electro-optical switching is mediated by surface plasmons, whose fields penetrate the LC by only a few hundred nanometers, the single-exponential relaxation dynamics naturally occurs [see Fig. 4(b)].

The simulated switching-on dynamics exhibit a wider range of the characteristic time scaling from a few microseconds at the grating to about 50 μs at 200 nm above it. This is a natural consequence of the rapid decrease of the driving electric field with increasing distance from the grating electrodes. Although the switching-on time further increases in the LC bulk, it cannot be visualized by the plasmon-mediated electro-optics.

VI. CONCLUSIONS

Low electro-optical switching speed is a key limitation of LC-based devices that prevents their extensive application in fields other than display technologies. A conventional LC cell having a thickness and a LC material similar to those used above exhibits electro-optical switching times of tens of milliseconds. One can speed up the switching on by using higher driving voltages; however, doing so leaves unaffected the switching-off relaxation, which is determined by the LC material properties and the LC cell dimensions [25,26]. Faster relaxation has been reported in, e.g., a composite material with LC-infiltrated polymer nanopores, but its noticeable switching requires voltages of a few hundred volts [40]. Ferroelectric liquid crystals (FLCs) that are known to switch faster (the times in the range 40–200 μs, depending on the viscosity and spontaneous polarization) also need strong electric fields: the classical FLC material ZLI-4655-100 from Merck switches over 42 μs at 20 °C [41], which, however, requires a driving voltage of ± 15 V per micrometer, and the switching is binary (no gray scale). In the latest studies of fast switchable FLC gratings, the switching time does not go below 100 μs under electric fields of 7 V/μm [42]. Using more sophisticated geometries, one can employ a nematic LC in, e.g., a dual-field mode, when switching on and switching off are both electrically driven. The overall switching time then can be pushed into the submillisecond range using reasonable driving voltages of about 10 V [43].

As we demonstrate in this paper, combining an ordinary LC material with a metal nanostructure allows one to obtain switching times below 100 μs with switching voltages of just a few volts. Compared to conventional LC electro-optical cells, this is an impressive improvement that demonstrates the advantages of plasmon-mediated LC electro-optics. Instead of manipulating the plane-wave propagation through the LC bulk, the engagement of plasmons here allows one to visualize the LC realignment within tiny surface layers, which react much faster and require lower driving voltages.

In order to show the benefits of the concept *per se*, we intentionally keep the hybrid system design simple in this paper. Nevertheless, at this first step, notably accelerated electro-optical light modulation is already realized. Next, straightforward system optimization can be performed, including a minimization of the background transmission, decreasing the thickness of the LC layer and employing more advanced LC mixtures. The 5% field-induced variation of the transmittance achieved thus far is not high enough to be applied directly in, for example, light modulators. However, a comparison of curves 4 and 5 in Fig. 7 shows that the modulation depth can be significantly increased (up to 15%) by ensuring planar LC alignment at the grating. Such an alignment was reported recently for nematic LC on gratings of shorter periods [18], and we see no reason why, by adjusting the FIB milling conditions and grating geometry, such alignment cannot be induced by gratings having (200–300)-nm periods. Note that doing so also boosts the relaxation speed as its time decreases as a square of the grating period [see Eq. (4) and the related discussion].

Besides the described plasmon-mediated transmittance modulation, one can also utilize the fast control over the light polarization by switching the LC director near the grating. In this case, a thicker metal grating can be used as both a driving electrode and an output polarizer blocking the TE-polarized light. In the field *on* state, the TE-polarized light incident from the LC side partially converts to the TM state while propagating through the strongly deformed surface LC layer, and only this part passes through the metal grating. Our preliminary simulations show that fast switching here over 50–100 μs between the deep, dark field *off* and bright field *on* states (with polarized light transmittance at the 30% level) can occur. Practical implementation of such a system is still technically challenging as one has to refine the fabrication technique to produce interdigitated nanogratings in relatively thick metal films and to ensure reliable planar LC alignment at those thicker gratings. Also, the use of LC materials with high birefringence (of about 0.4) is important in this case.

The specific design of the hybrid plasmonic-LC cell allows for nonstandard ways of optimizing other important characteristics. For instance, in conventional LC cells, the polarizers are distant from the LC layer. In order to improve the viewing angle range, one has to suppress the leaking of obliquely incident light through crossed polarizers as well as to compensate for the angular dependence of the optical delay in the LC layers. In our case, a thicker metal grating in direct contact with the LC layer can be employed as a polarizer. Doing so allows us to solve the viewing-angle problem by combining a collimated backlight source with a scattering nanorelief on the surface of a metal electrode system that omnidirectionally distributes the outgoing light.

To conclude, there are several routes to further increasing the speed and modulation depth and enhance other important functional parameters of the hybrid plasmonic-LC systems, and to develop ultrafast LC-based devices for diverse photonic applications.

ACKNOWLEDGMENTS

This work has been supported by the Russian Science Foundation (Project No. 14-12-00553). The work of V. V. A. and A. R. G. has been supported by the Russian Foundation for Basic Research (Project No. 16-29-11754 ofi_m). We are grateful to the IC RAS Shared Research Center (supported by the Ministry of Education and Science of the Russian Federation) for the equipment provided and to Mikhail Givargizov for the vacuum sputtering of metal films.

[1] K. Kneipp, M. Moskovits, and H. Kneipp, *Electromagnetic Theory of SERS* (Springer, New York, 2006).
[2] M. Kauranen and A. V. Zayats, Nonlinear plasmonics, Nat. Photonics **6**, 737 (2012).
[3] T. W. Ebbesen, H. J. Lezec, H. F. Ghaemi, T. Thio, and P. A. Wolff, Extraordinary optical transmission through sub-wavelength hole arrays, Nature (London) **391**, 667 (1998).
[4] J. A. Porto, F. J. Garcia-Vidal, and J. B. Pendry, Transmission Resonances on Metallic Gratings with Very Narrow Slits, Phys. Rev. Lett. **83**, 2845 (1999).
[5] C. Genet and T. W. Ebbesen, Light in tiny holes, Nature (London) **445**, 39 (2007).
[6] T. Xu, Y. K. Wu, X. Luo, and L. J. Guo, Plasmonic nanoresonators for high-resolution colour filtering and spectral imaging, Nat. Commun. **1**, 59 (2010).
[7] M. Decker, R. Zhao, C. M. Soukoulis, S. Linden, and M. Wegener, Twisted split-ring-resonator photonic metamaterial with huge optical activity, Opt. Lett. **35**, 1593 (2010).
[8] M. V. Gorkunov, A. A. Ezhov, V. V. Artemov, O. Y. Rogov, and S. G. Yudin, Extreme optical activity and circular dichroism of chiral metal hole arrays, Appl. Phys. Lett. **104**, 221102 (2014).
[9] Y. Tang and A. E. Cohen, Optical Chirality and Its Interaction with Matter, Phys. Rev. Lett. **104**, 163901 (2010).
[10] Y. Wang, J. Xu, Y. Wang, and H. Chen, Emerging chirality in nanoscience, Chem. Soc. Rev. **42**, 2930 (2013).
[11] *Nonlinear, Tunable and Active Metamaterials*, edited by I. V. Shadrivov, M. Lapine, and Yu. S. Kivshar (Springer, New York, 2015).
[12] T. J. Kim, T. Thio, T. W. Ebbesen, D. E. Grupp, and H. J. Lezec, Control of optical transmission through metals perforated with subwavelength hole arrays, Opt. Lett. **24**, 256 (1999).
[13] P. A. Kossyrev, A. Yin, S. G. Cloutier, D. A. Cardimona, D. Huang, P. M. Alsing, and J. M. Xu, Electric field tuning of plasmonic response of nanodot array in liquid crystal matrix, Nano Lett. **5**, 1978 (2005).
[14] S. Xiao, U. K. Chettiar, A. V. Kildishev, V. Drachev, I. C. Khoo, and V. M. Shalaev, Tunable magnetic response of metamaterials, Appl. Phys. Lett. **95**, 033115 (2009).

[15] A. Minovich, J. Farnell, D. N. Neshev, I. McKerracher, F. Karouta, J. Tian, D. A. Powell, I. V. Shadrivov, H. H. Tan, C. Jagadish, and Y. S. Kivshar, Liquid crystal based nonlinear fishnet metamaterials, Appl. Phys. Lett. **100**, 121113 (2012).

[16] O. Buchnev, J. Y. Ou, M. Kaczmarek, N. I. Zheludev, and V. A. Fedotov, Electro-optical control in a plasmonic metamaterial hybridised with a liquid-crystal cell, Opt. Express **21**, 1633 (2013).

[17] M. Decker, C. Kremers, A. Minovich, I. Staude, A. E. Miroshnichenko, D. Chigrin, D. N. Neshev, C. Jagadish, and Y. S. Kivshar, Electro-optical switching by liquid-crystal controlled metasurfaces, Opt. Express **21**, 8879 (2013).

[18] S. P. Palto, M. I. Barnik, V. V. Artemov, N. M. Shtykov, A. R. Geivandov, S. G. Yudin, and M. V. Gorkunov, Liquid crystal on subwavelength metal gratings, J. Appl. Phys. **117**, 223108 (2015).

[19] O. Buchnev, N. Podoliak, M. Kaczmarek, N. I. Zheludev, and V. A. Fedotov, Electrically controlled nanostructured metasurface loaded with liquid crystal: Toward multifunctional photonic switch, Adv. Opt. Mater. **3**, 674 (2015).

[20] D. Franklin, Y. Chen, A. Vazquez-Guardado, S. Modak, J. Boroumand, D. Xu, S. T. Wu, and D. Chanda, Polarization-independent actively tunable colour generation on imprinted plasmonic surfaces, Nat. Commun. **6**, 7337 (2015).

[21] J. D. Swalen and G. J. Sprokel, in *The Physics and Chemistry of Liquid Crystal Devices*, edited by G. J. Sprokel (Springer, New York, 1980).

[22] K. R. Welford, J. R. Sambles, and M. G. Clark, Guided modes and surface plasmon-polaritons observed with a nematic liquid crystal using attenuated total reflection, Liq. Cryst. **2**, 91 (1987).

[23] M. E. Caldwell and E. M. Yetman, Surface-plasmon spatial light modulators based on liquid crystal, Appl. Opt. **31**, 3880 (1992).

[24] P. G. de Gennes and J. Prost, *The Physics of Liquid Crystals* (Clarendon Press, Oxford, 1993).

[25] L. M. Blinov, *Structure and Properties of Liquid Crystals* (Springer, New York, 2011).

[26] M. Oh-e and K. Kondo, The in-plane switching of homogeneously aligned nematic liquid crystals, Liq. Cryst. **22**, 379 (1997).

[27] M. V. Gorkunov and M. A. Osipov, Tunability of wire-grid metamaterial immersed into nematic liquid crystal, J. Appl. Phys. **103**, 036101 (2008).

[28] S. P. Palto, M. I. Barnik, I. V. Kasyanova, A. R. Geivandov, N. M. Shtykov, V. V. Artemov, and M. V. Gorkunov, Plasmon electro-optic effect in a subwavelength metallic nanograting with a nematic liquid crystal, JETP Lett. **103**, 25 (2016).

[29] Q. Cao and P. Lalanne, Negative Role of Surface Plasmons in the Transmission of Metallic Gratings with Very Narrow Slits, Phys. Rev. Lett. **88**, 057403 (2002).

[30] B. Sturman, E. Podivilov, and M. Gorkunov, Theory of extraordinary light transmission through arrays of subwavelength slits, Phys. Rev. B **77**, 075106 (2008).

[31] K. M. McPeak, S. V. Jayanti, S. J. P. Kress, S.Meyer, S. Iotti, A. Rossinelli, and D. J. Norris, Plasmonic films can easily be better: Rules and recipes, ACS Photonics **2**, 326 (2015).

[32] I. H. Malitson, Interspecimen comparison of the refractive index of fused silica, J. Opt. Soc. Am. **55**, 1205 (1965).

[33] A. D. Rakic, A. B. Djurisic, J. M. Elazar, and M. L. Majewski, Optical properties of metallic films for vertical-cavity optoelectronic devices, Appl. Opt. **37**, 5271 (1998).

[34] J. Li, C. H. Wen, S. Gauza, R. Lu, and S. T. Wu, Refractive indices of liquid crystals for display applications, J. Disp. Technol. **1**, 51 (2005).

[35] S. H. Lee, S. L. Lee, and H. Y. Kim, Electro-optic characteristics and switching principle of a nematic liquid crystal cell controlled by fringe-field switching, Appl. Phys. Lett. **73**, 2881 (1998).

[36] S. H. Lee, H. Y. Kim, I. C. Park, Y. H. Lee, S. L. Lee, W. H. Choi, W. G. Lee, J. Y. Lee, J. S. Park, and C. H. Lee, Wide viewing angle, dual-domainlike VA-LCD, SID Int. Symp. Dig. Tech. Pap. **29**, 838 (1998).

[37] S. Pestov and V. Vill, in *Springer Handbook of Condensed Matter and Materials Data*, edited by W. Martienssen and H. Warlimont (Springer, Berlin 2005).

[38] S. P. Palto, A. R. Geivandov, I. V. Kasyanova, V. V. Artemov, and M. V. Gorkunov, Micro-and nanostructures for the spatially periodic orientation of liquid crystals obtained by focused ion beam milling, JETP Lett. **105**, 174 (2017).

[39] See https://optiwave.com/applications/fdtd-optical-grating-simulations-using-optifdtd.

[40] Y. Inoue, H. Yoshida, H. Kubo, and M. Ozaki, Deformation-free, microsecond electro-optic tuning of liquid crystals, Adv. Opt. Mater. **1**, 256 (2013).

[41] Merck GmbH, Ferroelectric smectic mixtures (1990).

[42] Y. Ma, X. Wang, A. K. Srivastava, V. G. Chigrinov, and H.-S. Kwok, Fast switchable ferroelectric liquid crystal gratings with two electro-optical modes, AIP Adv. **6** 035207 (2016).

[43] S. P. Palto, M. I. Barnik, A. R. Geivandov, I. V. Kasyanova, and V. S. Palto, Submillisecond inverse TN bidirectional field switching mode, J. Disp. Technol. **12**, 992 (2016).